1.2 Nanotube Membrane Sensors: Resistive Sensing and Ion Channel Mimetics

M. WIRTZ and C. R. MARTIN
Department of Chemistry and Center for Chemical Research
at the Bio/Nano Interface, University of Florida, Gainesville, USA

Abstract

Nanotubule membranes are utilized for sensing applications and ion channel mimetics. The nanotubule membranes are composed of either gold or alumina. The gold nanotubule membranes are prepared via electroless deposition of Au on to the pore walls of a polycarbonate membrane, ie, the pores act as templates for the nanotubes. These membranes are a new class of molecular sieves and can be used to separate small molecules on the basis of molecular size. In addition, the use of these membranes in new approaches to electrochemical sensing is discussed. In this case, a current is forced through the nanotubes, and analyte molecules present in a contacting solution phase modulate the value of this transmembrane current. We further discuss synthetic micropore and nanotube membranes that mimic the function of a ligand-gated ion channel, ie, these membranes can be switched from an 'off' state (no or low ion current through the membrane) to an 'on' state (higher ion current) in response to the presence of a chemical stimulus, eg, drug or surfactant. Ion channel mimics are based on both modified Au nanotube and microporous alumina membranes.

Keywords: Nanotubule membranes; resistive sensing; ion channel mimetics; electroless deposition; molecular sieving; ion current; ion channel pores

Contents

1.2.1 Introduction

We have been exploring the transport and electrochemical properties of nanotube membranes prepared by the template method [1–3], a general approach for preparing nanomaterials. This method entails the synthesis or deposition of the desired material within the cylindrical and monodisperse pores of a nanopore membrane or other solid. We have used polycarbonate filters, prepared via the track-etch method [4], and nanopore aluminas, prepared electrochemically from Al foil [5], as our template materials. Cylindrical nanostructures with monodisperse diameters and lengths are obtained and, depending on the membrane and synthetic method used, these may be solid nanowires or hollow nanotubes. We, and others, have used this method to prepare nanowires and tubes composed of metals [5–15], polymers [16–19], semiconductors [20, 21], carbons [22–24], and Li^+ inter-

calation materials [25–27]. It is also possible to prepare composite nanostructures, both concentric tubular composites, where an outer tube of one material surrounds an inner tube of another [28, 29], and segmented composite nanowires [30].

One of our earliest applications of the template method was to prepare ensembles of microscopic [31, 32] and nanoscopic [33, 34] electrodes. Such electrodes are prepared by depositing noble metals within the pores of the polycarbonate filtration membranes. Initially, we deposited the metal in the pores using electrochemical plating methods [31], but we ultimately discovered that electroless plating allowed for more uniform metal deposition [33]. In the electroless method, metal deposition begins at the pore walls, creating, at short deposition time, hollow metal nanotubes within the pores [8–12, 35, 36].

Coincidentally, there is also a long-standing interest in our research group in the area of membrane-based chemical separations [37–39]. This interest led us to undertake a series of fundamental investigations of the transport properties of gold nanotube membranes. We discovered that by controlling the deposition time, we could prepare Au nanotubes that had effective inside diameters of molecular dimensions (<1 nm) [9]. This suggested that these membranes might be useful as molecular sieves. In addition, because these membranes are composed of an electronically conductive material, it occurred to us that excess charge could be applied to the tubes by electrochemical charging in an electrolyte solution. We reasoned that it might be possible to use this excess charge to regulate ion transport across these membranes [8, 35]. Furthermore, because the tubes are composed of gold, it seemed possible that we could use well-known Au–thiol chemistry to change the chemical environment within the tubes and, via this route, introduce chemical transport selectivity into these membranes [10–12, 36].

Another application for these nanotube membranes is in electroanalytical chemistry where the membrane is used to sense analyte species [40, 41]. In that work, membranes containing gold nanotubes with inside diameters that approached molecular dimensions (1–4 nm) were used [40]. The Au nanotube membrane was placed between two salt solutions and a constant transmembrane potential was applied. The resulting transmembrane current, associated with migration of ions through the nanotubes, was measured. When an analyte molecule whose diameter was comparable to the inside diameter of the nanotubes was added to one salt solution, this molecule partitioned into the nanotubes and partially occluded the pathway for ion transport. This resulted in a decrease in the transmembrane ion current, and the magnitude of the drop in current was found to be proportional to the concentration of the analyte [40].

In the experiment discussed above, a baseline transmembrane ion current was established, and the analyte molecule, in essence, turned off this current. It occurred to us that there might be an advantage in doing the opposite, ie, starting with an ideally zero current situation and having the analyte molecule switch on the ion current. That is, we would like to make a synthetic membrane that mimics the function of a ligand-gated ion channel. An example is the acetylcholine-gated ion channel [42], which is closed (‘off’ state) in the absence of acetylcholine but opens (and supports an ion current, ‘on’ state) when acetylcholine binds to the channel. In order

to accomplish this, the 'off' state was obtained by making gold and alumina membranes hydrophobic, and the 'on' state was obtained by introducing ions and electrolyte into the membrane [43]. Ions were introduced by either partitioning a hydrophobic ionic species (eg, a drug or a surfactant) into the membrane or by deprotonation of a surface-bound hydrophobic carboxylic acid.

In this chapter we discuss the use of the nanotube membranes as molecular sieves, chemical sensors, and synthetic ion channel mimics. We begin by briefly reviewing some of the experimental details such as the electroless plating method and the gas flux method used to determine nanotube inside diameter of gold nanotubule membranes. We then discuss investigations of molecular size-based transport selectivity in this type of membrane. This is followed by a discussion of an extremely sensitive chemical sensing method utilizing the Au nanotube membranes. Lastly, we describe alumina and gold nanotube membranes that mimic ligand-gated ion channels. In these modified membranes the current can be switched on by surfactants or drugs.

1.2.2 Membrane Preparation and Analysis

1.2.2.1 Template Membranes and Electroless Plating

Commercially available 'track-etched' polycarbonate filters are used as the templates to prepare the Au nanotubes. The track-etch process [4] entails bombarding a solid material (in this case a ca. 10 μm thick polycarbonate film) with a collimated beam of high-energy nuclear fission fragments to create parallel damage tracks in the film. The damage tracks are then etched into monodisperse cylindrical pores by exposing the film to a concentrated solution of aqueous base. The diameter of the pores is determined by the etch time and the etch solution temperature. The density of pores is determined by exposure time to the fission-fragment beam. Membranes with pore diameters ranging from as small as 10 nm to as large as ca. 10 μm are available commercially.

The membranes used for these studies had nominal pore diameters of 30 nm and contained 6×10^8 pores per cm^2 of membrane surface area. The nominal pore diameter (supplied by the manufacturer) was obtained from scanning electron microscopic images of the film surface. Microscopic investigations of template-synthesized nanostructures prepared within the pores of such membranes have shown that the diameter of the pore in the center of the membrane is larger than the diameter at the membrane surface, ie, that cigar-shaped pores are obtained [14, 17]. It has been suggested that this pore geometry arises because the fission fragment that creates the damage track also generates secondary electrons, which contribute to the damage along the track [14]. The number of secondary electrons generated at the faces of the membrane is less than in the central region of the membrane, and this is why 'bottleneck' pores are obtained.

The electroless plating method used to deposit the Au nanotubes [11, 33] within the pores of these membranes (Figure 1.2.1). Briefly, the template membrane is first 'sensitized' by immersion in $SnCl_2$ solution, which results in deposition of Sn(II) on all of the membrane's surfaces (pore walls and membrane faces). The sensitized membrane is then immersed in $AgNO_3$ solution, and a surface redox reaction occurs (Equation (1.2.1)) which yields nanoscopic metallic Ag particles on the membrane surfaces:

$$Sn(II)_{surf} + 2Ag(I)_{aq} \rightarrow Sn(IV)_{surf} + 2Ag(0)_{surf} \quad (1.2.1)$$

where the subscripts surf and aq denote species adsorbed on the membrane surfaces and species dissolved in solution, respectively. The membrane is then immersed in a commercial gold plating solution and a second surface redox reaction occurs, to yield Au nanoparticles on the surfaces:

$$Au(I)_{aq} + Ag(0)_{surf} \rightarrow Au(0)_{surf} + Ag(I)_{aq} \quad (1.2.2)$$

These surface-bound Au nanoparticles are good autocatalysts for the reduction of Au(I) to Au(0) using formaldehyde as the reducing agent. As a result, Au deposition begins at the pore walls, and Au tubes are obtained within the pores (Figure 1.2.2) [8–12, 35, 36). In addition, the faces of the membrane become coated with thin Au films. These surface films do not, however, block the mouths of the nanotubes, and there are open nanoscopic channels running from one face of the membrane to the other. By controlling the electroless plating time, the inside diameter of these nanotubes can be controlled at will, down to molecular dimensions.

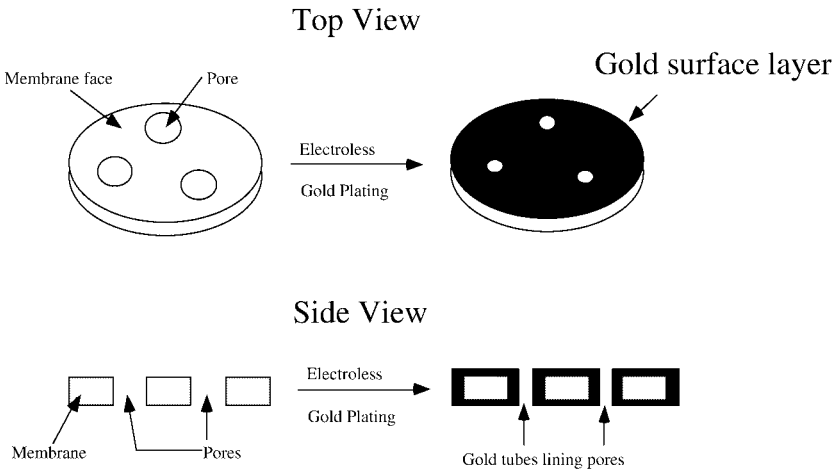

Figure 1.2.1. Schematic of the electroless plating process used to prepare the Au nanotube membranes.

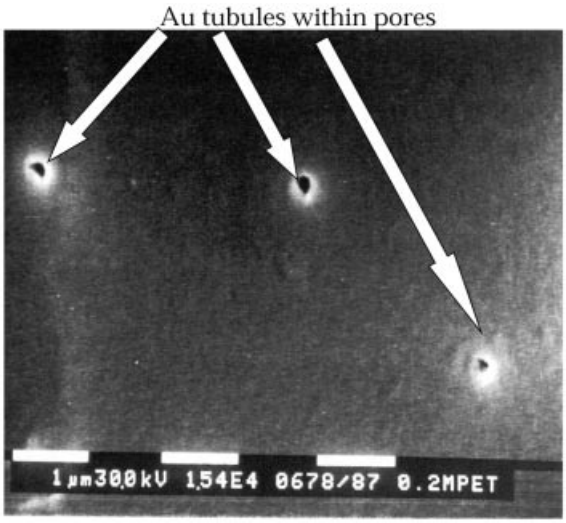

Figure 1.2.2. Scanning electron micrograph of the surface of a polycarbonate template membrane showing three Au nanotubes deposited within the pores. To visualize the tubes by scanning electron microscopy, the membrane had larger pores than those used to prepare the nanotube membranes discussed here.

1.2.2.2 Estimation of the Nanotube Inside Diameter

We use a gas-transport method to obtain an estimate of the inside diameter (id) of the template-synthesized Au nanotubes [11]. Briefly, the tube-containing membrane is placed in a gas-permeation cell, and the upper and lower half-cells are evacuated. The upper half-cell is then pressurized, typically to 20 psi with H_2, and the pressure–time transient associated with leakage of H_2 through the nanotubes is measured using a pressure transducer in the lower half-cell. The pressure–time transient is converted to gas flux (Q, mol s^{-1}) which is related to the radius of the nanotubes (r, cm) via [11, 44]

$$Q = 4/3(2\pi/MRT)^{1/2}(nr^3\Delta P/l) \tag{1.2.3}$$

where ΔP is the pressure difference across the membrane (dyn cm^{-2}), M is the molecular weight of the gas, R is the gas constant (erg K^{-1} mol^{-1}), n is the number of nanotubes in the membrane sample, l is the membrane thickness (cm), and T is the temperature (K). At long plating times, membranes containing nanotubes with ids of molecular dimensions are obtained (Figure 1.2.3).

In using Equation (1.2.3) we assume (1) that we know the number of nanotubes (n) in the membrane sample, (2) that the nanotubes have a constant inside diameter down their entire length, and (3) that the mechanism of gas transport through the membrane is Knudsen diffusion in the nanotubes. We have discussed the validity of each of these assumptions in detail in a recent review [45].

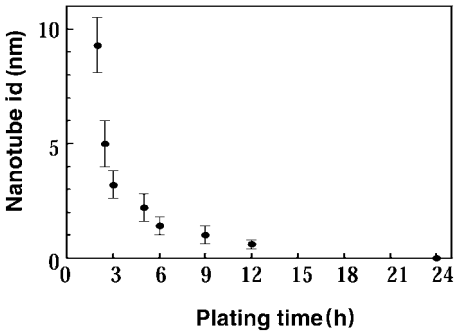

Figure 1.2.3. Variation of the nanotube effective inside diameter with plating time.

1.2.3 Molecular Sieving and Filtration in Au Nanotube Membranes

Molecular sieving experiments were conducted using a simple U-tube permeation cell, where the membrane to be studied separates the 'feed' and 'permeate' half-cells. The feed half-cell is an aqueous solution containing the molecule or molecules whose transport properties are to be evaluated. The permeate half-cell initially contains only water or a salt solution. Passive diffusion drives the permeate molecule from the feed half-cell through the membrane and into the permeate half-cell. The time course of the transport process is followed by periodically assaying the permeate half-cell for the permeate molecule(s). The transport data are plotted as moles of permeate molecules transported against permeation time [9–12]. Straight-line plots are typically obtained, and the flux of the permeate molecule can be calculated from the slope. We will call such plots 'flux plots' in this chapter.

1.2.3.1 Molecular Sieving in Single-molecule Permeation Experiments

In these experiments, the flux plot for a particular molecule is determined with only that molecule present in the feed solution. The feed solution is then replaced with a solution of a second molecule and the flux plot for this molecule is obtained for the same membrane. A membrane-transport selectivity coefficient (α) can then be obtained by ratioing the fluxes for the two permeate molecules. Since molecular size-based selectivity is of interest here, one of the permeate molecules used was large, the tris-bipyridyl complex of Ru(II), $Ru(bpy)_3^{2+}$, and the other was smaller, methyl viologen, MV^{2+} (Figure 1.2.4).

The ratio of the diffusion coefficients for MV^{2+} and $Ru(bpy)_3^{2+}$ in free aqueous solution is 1.5 [40, 45, 46]. For this reason, if a simple solution-like diffusion process were operative in the nanotubes, a selectivity coefficient of $\alpha = 1.5$ would be anticipated. In contrast, even for the largest id nanotubes investigated

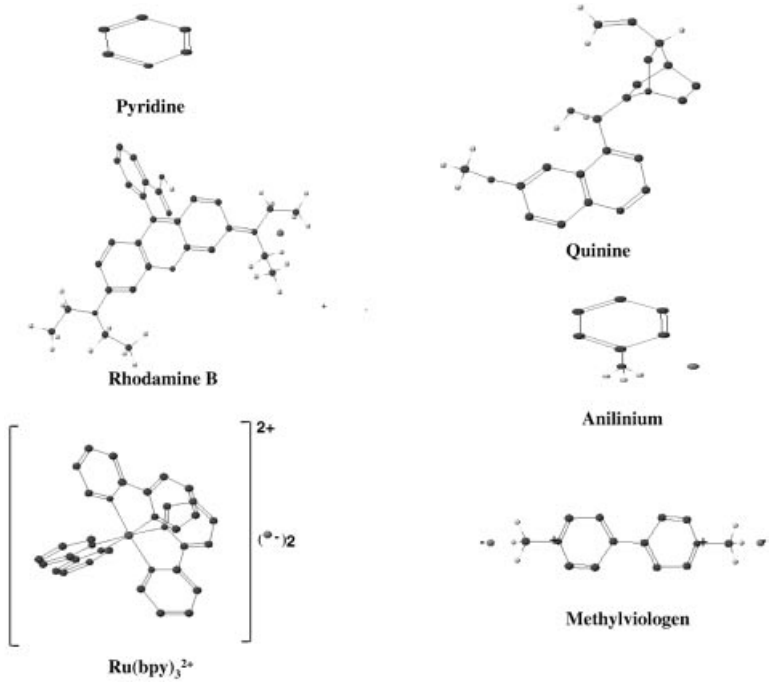

Figure 1.2.4. Chemical structures and approximate relative sizes of the three big molecule–small molecule pairs used in the molecular filtration experiments. Quinine, MV^{+2}, and $Ru(bpy)_3^{+2}$ were also used as analytes in the sensor work.

(5.5 nm), the selectivity coefficient was substantially greater, $\alpha = 50$ (Figure 1.2.5 a) [9]. These data show that size-based molecular sieving occurs in these large-id (larger than molecular dimensions) nanotubes.

Molecular sieving is a result of hindered diffusion of the molecules in the Au nanotubes [47]. The simplest way to understand hindered diffusion is to consider first the Stokes–Einstein equation that relates the diffusion coefficient (D_s) to the molecular radius (r_m) for diffusion in free solution:

$$D_s = kT/6\pi\eta\rho r_m \tag{1.2.4}$$

where k is the Boltzmann constant, T is the absolute temperature, and η is the viscosity. The denominator $6\pi\eta\rho r_m$ can be thought of as a molecular-friction coefficient that determines the resistance to diffusion in the solution. As would be expected, this molecular-friction term increases with increasing size of the molecule and increasing viscosity of the solution.

In the Au nanotube membranes, this molecular-friction coefficient is larger than in free solution because collisions with the nanotube wall increase the frictional drag on the molecule [44]. In addition, the rate of diffusive mass transport in the nanotube is decreased, relative to a contacting solution phase, because of

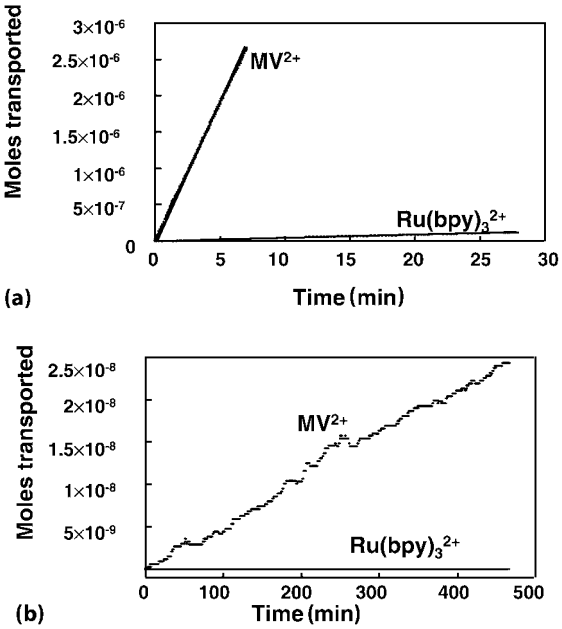

Figure 1.2.5. Single-molecule permeation experiments showing moles of MV^{2+} and $Ru(bpy)_3^{2+}$ transported versus time. Membranes contained nanotubes with id (**a**) 5.5 and (**b**) <0.6 nm. Only MV^{2+} was transported through this membrane.

steric reasons [47]. Consider a molecule of radius r_{mol} diffusing within a nanotube of comparable radius r_{tube}. The extent to which the diffusion coefficient for a molecule in the nanotube (D_{tube}) is decreased relative to its value in free solution (D_{sol}) is related to the parameter λ, which is the ratio of the radius of the diffusing molecule to the radius of the nanotube [47]:

$$\lambda = r_{mol}/r_{tube} \tag{1.2.5}$$

A large number of theoretical expressions have been derived that predict how the ratio D_{tube}/D_{sol} varies with λ [44, 47, 48]. The extremes are easy to define: when $\lambda = 0$ ($r_{mol} << r_{tube}$) $D_{tube}/D_{sol} = 1$, and when λ approaches unity (tube and molecule are the same size) D_{tube}/D_{sol} must approach zero. The Renkin equation:

$$D_{tube}/D_{sol} = 1 - 2.104\lambda + 2.09\lambda^3 - 0.95\lambda^5 \tag{1.2.6}$$

is an often-used example of the relationship between D_{tube}/D_{sol} and λ [48]. Plots of this equation and various other expressions for the relationship between D_{tube}/D_{sol} and λ can be found in the literature [44, 47, 48].

Equations (1.2.5) and (1.2.6) show that for any nanotube id, diffusivity in the nanotube membrane will be lower for the larger $Ru(bpy)_3^{2+}$ than for the smaller MV^{2+}. This is reflected in the transport data, where the flux of the larger

$Ru(bpy)_3^{2+}$ is decreased more than the flux for the smaller MV^{2+}. As a result, $\alpha = 50$ is obtained [9]. Equations (1.2.5) and (1.2.6) predict that as the nanotube id is made smaller, the α value should become even larger, which is also reflected in the transport data. Values for the 5.5, 3.2 and 2.0 nm id nanotube membranes are $\alpha = 50$, 88, and 172, respectively [9].

1.2.3.2 Molecular Filtration in Two-molecule Permeation Experiments

The smallest id nanotube membrane investigated (id $\approx$ 0.6 nm) provides a measurable flux for MV^{2+}, but the larger $Ru(bpy)_3^{2+}$ could not be detected in the permeate solution, even after a 2 week permeation experiment (Figure 1.2.5 b). These data suggest that clean separation (molecular filtration) of these two species should be possible with this nanotube membrane. This was proved by doing two-molecule permeation experiments, where both the larger and smaller molecules (Figure 1.2.4) were present in the feed half-cell together. A simple U-tube cell was used, and the permeate solution was periodically assayed, using UV–vis absorption or fluorescence, for both molecules. For all three of the large molecule–small molecule pairs shown in Figure 1.2.4, the small molecule could be easily detected in the permeate solution but the large molecule was undetectable [9].

These data show that within the limits of the measurement, the Au nanotube membrane can cleanly separate large molecules from small molecules. However, one could argue that the large molecule is, indeed, present in the permeate solution but at a concentration just below the detection limit of the analytical method employed. This argument allows us to define a minimum transport selectivity coefficient (α_{min}) for each small molecule–large molecule pair investigated, where α_{min} is defined as the measured concentration of the small molecule in the permeate solution divided by the detection limit for the large molecule. The α_{min} values obtained are extraordinary (Table 1.2.1). It is important to stress again that, in all three cases, the larger molecule was undetectable in the permeate solution.

Table 1.2.1. Minimal membrane transport selectivity coefficients

Permeate pair	α_{min}
Pyridine–quinine	15 000
Anilinium–rhodamine B	130 000
MV^{2+}–$Ru(bpy)_3^{2+}$	1 500

1.2.4 Chemical Sensing with Au Nanotube Membranes

In addition to the above possible applications in size-based separations, these Au nanotube membranes have been used as sensors for the determination of ultra-trace concentrations of ions and molecules [40, 41, 46]. In this case, the nanotube membrane was allowed to separate two salt solutions, a constant transmembrane potential was applied, and the resulting transmembrane current was measured. When an analyte with dimensions comparable to the inside diameter of the nanotubes was added to one of the salt solutions, a decrease in transmembrane current was observed. The magnitude of this drop in transmembrane current (Δi) is proportional to the analyte concentration.

1.2.4.1 Calibration Curves and Detection Limits

As in the transport experiments, a U-tube cell was assembled with the nanotube membrane separating the two halves of the cell. The two half-cells were filled with the desired electrolyte and an electrode was placed in each half-cell. Three different sets of electrodes and electrolytes were used. The first set consisted of two Pt plate electrodes, and the electrolyte used in both half-cells was 0.1 M KF. The second set consisted of two Ag/AgCl wires, and the electrolyte used in both half-cells was 0.1 M KCl. The third set consisted of two Ag/AgI wires immersed in 0.1 M KI.

As noted above, the experimental protocol used with these cells was to immerse the electrodes into the appropriate electrolyte and apply a constant potential between the electrodes. The resulting transmembrane current was measured and recorded on an *X–t* recorder. After obtaining this baseline current, the anode half-cell was spiked with a known quantity of the desired analyte (Figure 1.2.4). This resulted in a change in the transmembrane current, Δi (Figure 1.2.6). A potentiostat was used to apply the potential between the electrodes and measure the transmembrane current. The transmembrane potential used was on the order of 0.5 V [40, 46].

Plots of log Δi versus log [analyte] for the analytes $Ru(bpy)_3^{2+}$, MV^{2+}, and quinine (Figure 1.2.4) were obtained using Ag/AgCl electrodes and 0.1 M KCl as the electrolyte in both half-cells (Figure 1.2.7). For these experiments, a membrane with 2.8 nm id Au nanotubes was used. A log–log format is used for these 'calibration curves' because of the large dynamic range (spanning as much as five orders of magnitude in analyte concentration) obtained with this cell. Analogous calibration curves were obtained for the other electrode/electrolyte systems investigated. The detection limits [40] obtained are shown in Table 1.2.2. For the divalent cationic electrolytes, the detection limits were lowest (best) in the Ag/AgI/KI cell and worst in the Pt/KF cell. The detection limit for quinine was the same in both the Ag/AgI/KI and Ag/AgCl/KCl cells. In general, the detection limit decreases as the size of the analyte molecule increases (see Figure 1.2.4).

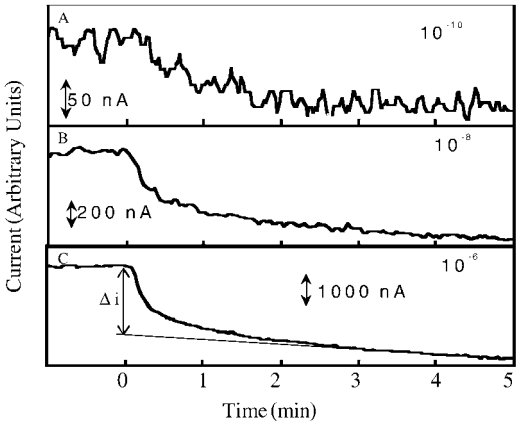

Figure 1.2.6. Nanotube membrane sensor current–time transients associated with spiking the anode half-cell with the indicated concentrations of $Ru(bpy)_3^{2+}$. Tube id=2.8 nm; Ag/AgCl/KCl cell; Δi determined as shown in (C).

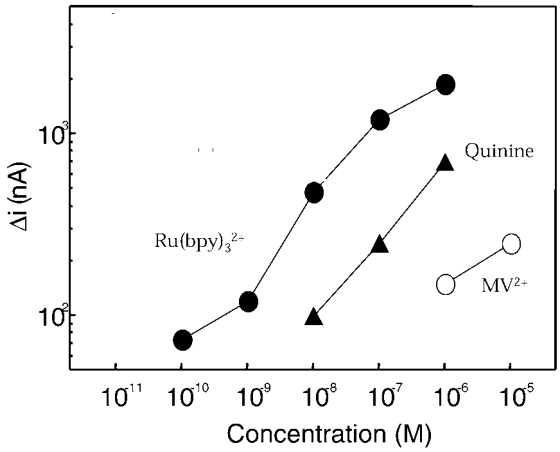

Figure 1.2.7. Calibrations curves for the indicated analytes. Membrane and cell as described in Figure 1.2.6.

Finally, the detection limits obtained (down to 10^{-11} M) are extraordinary and compete with even the most sensitive of modern analytical methods.

The majority of the quinine in both the KCl and KI solutions is present as the monoprotonated (monocationic) form. Perhaps the reason why the detection limits for $Ru(bpy)_3^{2+}$ and MV^{2+} are lower in the Ag/AgI/KI cell whereas the detection limit for quinine is the same in both this cell and the Ag/AgCl/KCl cell has to do with the difference in charge of these analytes (predominantly monocationic versus dicationic). To explore this point, the detection limits for a neutral

Table 1.2.2. Detection limits obtained for the three different electrode–electrolyte systems studied (nanotubule id = 2.8 nm)

Cell	Analyte	Detection limit (M)
Pt/KF	$Ru(bpy)_3^{2+}$	10^{-9}
Ag/AgCl/KCl	$Ru(bpy)_3^{2+}$	10^{-10}
	Quinine	10^{-8}
	MV^{2+}	10^{-6}
	2-Naphthol	10^{-6}
Ag/AgI/KI	$Ru(bpy)_3^{2+}$	10^{-11}
	Quinine	10^{-8}
	MV^{2+}	10^{-7}
	2-Naphthol	10^{-6}

analyte, 2-naphthol, were obtained in both the Ag/AgI/KI and Ag/AgCl/KCl cells. Like quinine, the detection limit for this neutral analyte was the same in both cells (10^{-6} M, Table 1.2.2).

In the membrane transport studies it was shown that $Ru(bpy)_3^{2+}$ and MV^{2+} come across such membranes as the ion multiples $Ru(bpy)_3^{2+}(X^-)_2$ and $MV^{2+}(X^-)_2$ (X^- = anion) [9]. In the KI cell, the ion multiple contains two larger (relative to chloride) iodide anions. Perhaps the larger size of the iodide ion multiple accounts for the lower detection limit in the KI-containing cell. If this is true then the difference between the quinine cation paired with one I^- versus this cation paired with one Cl^- is not great enough to cause the detection limit for this predominantly monovalent analyte to be significantly different in the Ag/AgI/KI versus the Ag/AgCl/KCl cells (Table 1.2.2).

The final variable to be investigated is the effect of nanotube inside diameter on detection limit. To explore this parameter, membranes with nanotube inside diameters of approximately of 3.8, 2.8, 2.2, 1.8, and 1.4 nm were prepared and used in the Ag/AgI/KI cell [40]. Calibration curves for the analytes $Ru(bpy)_3^{2+}$, MV^{2+}, and quinine were generated as before, and detection limits were obtained from these calibration curves. Figure 1.2.8 shows plots of detection limits for these three different analytes versus the nanotube inside diameter in the membrane used. A minimum in this plot is observed for each of the three analytes.

The nanotube membrane that produces the minimum (best) detection limit depends on the size of the analyte. These molecules decrease in size in the order $Ru(bpy)_3^{2+}$ > quinine > MV^{2+}. The nanotube membrane that yields the lowest detection limit follows this size order, that is, the nanotube diameters that produce the lowest detection limit for $Ru(bpy)_3^{2+}$, quinine, and MV^{2+} are 2.8, 2.2, and 1.8 nm, respectively. For the roughly spherical analytes, the optimum tube diameter is slightly over twice the diameter of the molecule.

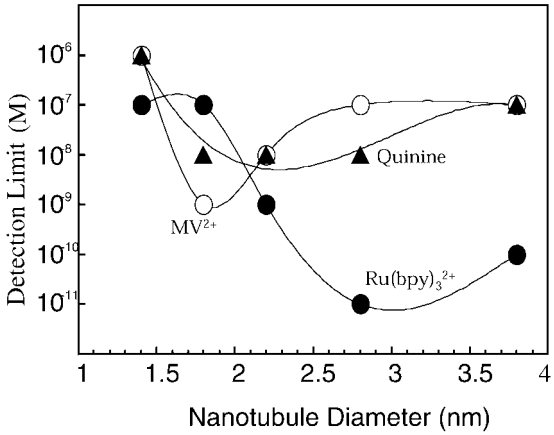

Figure 1.2.8. Detection limits for MV^{2+}, quinine, and $Ru(bpy)_3^{2+}$ versus id of the nanotubes used in the sensor.

1.2.4.2 Molecular Size based Selectivity

The data presented above show a strong correlation between detection limit and the relative sizes of the nanotube and the analyte molecule (Figure 1.2.8). This indicates that this device should show molecular size-based selectivity. This is not surprising given the transport studies discussed previously. To explore size-based selectivity, a series of solutions were prepared containing decreasing concentrations of the analyte species, but containing a constant (higher) concentration of an interfering species. The interfering species was smaller than the analyte species. The response of the nanotube membrane (nanotube diameter = 2.8 nm) to these solutions was then measured starting from lowest to highest concentration of the analyte species.

The small pyridine molecule was used as the first interfering species. When present at a concentration of 10^{-4} M, pyridine offered very little interference for any of the analytes $Ru(bpy)_3^{2+}$, MV^{2+}, or quinine. The detection limits in the presence of 10^{-4} M pyridine were 10^{-10} M for $Ru(bpy)_3^{2+}$, 10^{-6} M for MV^{2+}, and 10^{-7} M for quinine, within an order of magnitude of the detection limit with no added interfering species (Table 1.2.2). Put another way, this nanotube membrane sensor can detect 10^{-10} M $Ru(bpy)_3^{2+}$ in the presence of six orders of magnitude higher pyridine concentration.

A second set of experiments was done using the larger MV^{2+} as the interfering species. Now at low concentrations of analyte, there is a region where the device produces a constant response due to the constant concentration (10^{-4} M) of this interfering species, ie, the much higher concentration of the MV^{2+} swamps the response of the device. However, as the concentration of $Ru(bpy)_3^{2+}$ increases, there is a concentration range where the device responds to this analyte species without interference from the MV^{2+}. This concentration range begins at concen-

trations of $Ru(bpy)_3^{2+}$ above 10^{-8} M. That is, the size-based selectivity is such that the larger analyte species, $Ru(bpy)_3^{2+}$, can be detected down to 10^{-8} M in the presence of four orders of magnitude higher concentration of the smaller interfering species, MV^{2+}.

These data can be quantified by defining the selectivity coefficient $K_{bpy/MV}$ as the slope of the calibration curve for the analyte, $Ru(bpy)_3^{2+}$, divided by the slope for the interfering species, MV^{2+}. This analysis is problematic because the calibration curves are nonlinear and because the device is not very sensitive to MV^{2+} [40]. However, taking the data from the central part of the $Ru(bpy)_3^{2+}$ calibration curve gives a slope of ~ 400 A M^{-1}; dividing by the slope for the MV^{2+} data gives $K_{bpy/MV} = 4000$. These experiments show that, in agreement with the transport studies, the nanotube membrane-based sensor can show excellent size-based selectivity.

1.2.5 Synthetic Ion Channel Pores

We have conducted experiments that provide proof of the basic concept that an analyte molecule can switch on an ion current in a synthetic membrane-based ion channel mimic [43]. The membrane used for most experiments was a commercially available microporous alumina filter. The pores in this membrane were made hydrophobic by reaction with an 18-carbon (C_{18}) alkylsilane. When placed between two salt solutions, the pores in this C_{18}-derivatized membrane are not wetted by water, yielding the 'off' state of the membrane. When exposed to a solution containing a sufficiently high concentration of a long-chain ionic surfactant (the analyte), the surfactant molecules partition into the hydrophobic membrane, and ultimately cause the pores to flood with water and electrolyte. As a result, the membrane will now support an ion current, and the ion channel-mimetic membrane is switched to its 'on' state. Cationic drug molecules can also switch this membrane from the off to the on state. Furthermore, when a hydrophobic –COOH-containing silane is used, the off/on transition can be induced by controlling the pH of the contacting solution phases.

1.2.5.1 Membrane Preparation

The alumina membranes were Anopore® (Whatman, Clifton, NJ, USA) that had nominally 200 nm diameter pores and were 60 μm thick (Figure 1.2.9). The alumina membranes were modified with octadecyltrimethoxysilane [43]. Alumina membranes were also derivatized with a silane that terminated with the 20-carbon carboxylic acid $–(CH_2)_{20}–COOH$. For the latter modification, a two-step method based on a literature procedure was used [43, 49, 50].

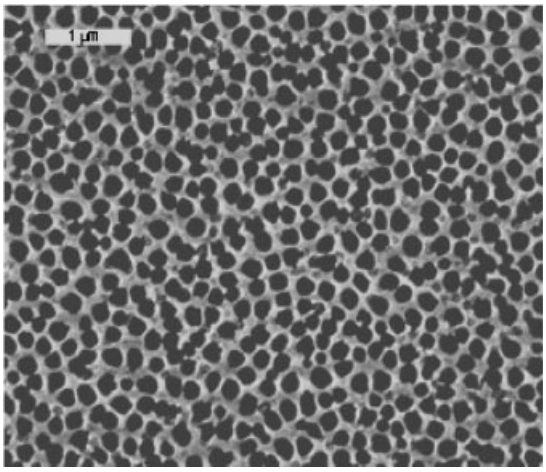

Figure 1.2.9. Scanning electron micrograph of the surface of an Anopore® alumina membrane.

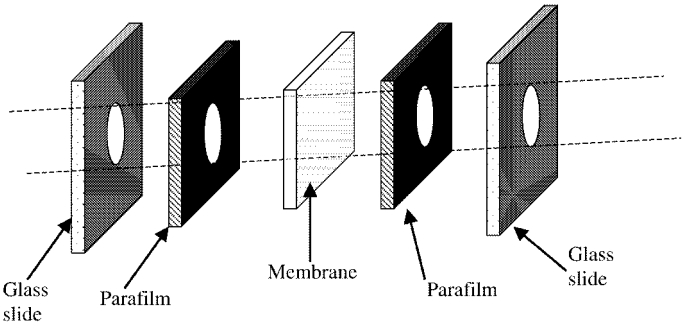

Figure 1.2.10. Membrane assembly.

Following attachment of the desired silane, the membrane was mounted into the assembly device shown in Figure 1.2.10. After assembling the various components, the assembly was heated for 3 min at 150 °C in an oven to melt the Parafilm, which acted as a glue to hold the various pieces together. This assembly exposes 0.079 cm^2 of membrane area to the contacting electrolyte solutions. We also conducted experiments with gold nanotube membranes containing nanotubes with inside diameters of ~ 2 nm. The Au nanotubule membranes were rendered hydrophobic by chemisorbing octadecanethiol to the nanotube walls [9].

1.2.5.2 AC Impedance Experiments with 1-Dodecanesulfonic Acid (DBS) Analyte

The membrane assembly was mounted between the halves of a U-tube permeation cell, and both half-cells were filled with ~ 20 mL of 0.1 M KCl. An Ag/AgCl working electrode was immersed in one half-cell solution, and a Pt counter electrode and an Ag/AgCl reference electrode were placed in the other half-cell [51–53].

AC Impedance measurements proved to be a useful way to demonstrate the analyte-induced switching of the membrane between the off and on states. The uppermost curve in Figure 1.2.11 is the Nyquist plot for a C_{18}-modified alumina membrane with 0.1 M KCl solutions, and no analyte (DBS), on either side of the membrane. As in prior investigations of ion channel and ion channel mimetic membranes [54, 55], the impedance data were interpreted in terms of the equivalent circuit shown in the inset in Figure 1.2.11, where R_s is the solution resistance, R_m is the membrane resistance, and C is the membrane capacitance. The dashed curve is the best fit to the experimental data, from which the R_m (Figure 1.2.12) and C values were obtained. Also shown in Figure 1.2.11 are impedance data after spiking the half-cell electrolyte solutions to the indicated concentrations with the analyte (DBS).

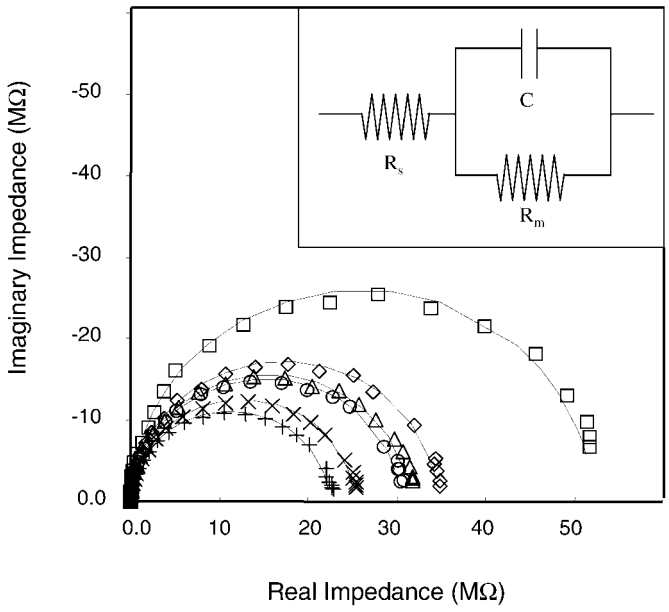

Figure 1.2.11. Nyquist plots for a C_{18}-modified alumina membrane upon exposure to increasing concentrations of DBS in 0.1 M KCl. The points are the experimental data. The lines are calculated data obtained using the equivalent circuit shown in the inset. Concentrations of DBS were as follows: □, 0; ◆, 1.4; △, 3; ○, 10; ×, 40; +, 100 nM.

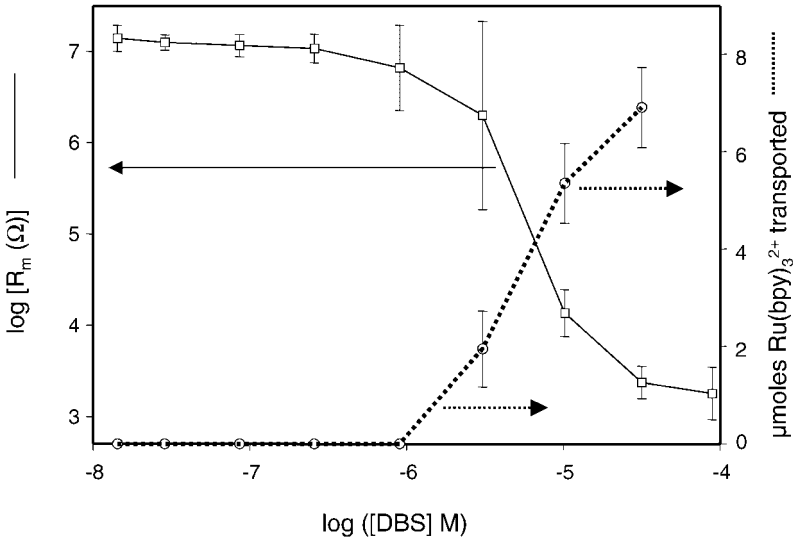

Figure 1.2.12. Plots of log (membrane resistance) (left *y*-axis) and μmoles of $Ru(bpy)_3^{2+}$ transported across the membrane (right *y*-axis) versus log[DBS] for a C_{18}-modified alumina membrane. The error bars represent the standard deviation of three separate experiments.

In the absence of DBS, the membrane resistance is very large, >50 MΩ as opposed to ∼ 5 Ω for the alumina membrane before modification with the C_{18} silane. Transport experiments (see below) show that this is because the very hydrophobic C_{18}-modified pores are not wetted by water. This is supported by contact angle measurements on the membrane surface, where a water contact angle of 130 $(\pm 8)^\circ$ was obtained for the C_{18}-treated alumina membrane as opposed to ∼ 8 $(\pm 1)^\circ$ for the untreated membrane. It should be noted that our C_{18}-treated alumina water contact angle is slightly higher than literature values, which are around 110° [56, 57]. This is presumably due to the increased roughness of the alumina surface.

While over the concentration range 10^{-9}–10^{-7} M there is some drop in membrane resistance with increasing DBS concentration (Figure 1.2.13), R_m remains very large (>20 MΩ). However, over the DBS concentration range between 10^{-6} and 10^{-5} M there is a precipitous, four orders of magnitude, drop in R_m (Figure 1.2.12). This drop signals the analyte-induced switching of the membrane from the off to the on states. The capacitance data also show the effect of this off/on transition. At concentrations of DBS below the transition, the membrane capacitance is extremely low (eg, 0.46 nF per cm^2 of membrane surface area at a DBS concentration of 10^{-6} M), but jumps by two orders of magnitude when the membrane is switched to the on state (22 nF per cm^2 at [DBS] = 10^{-5} M). We note that the switching concentration of DBS is much lower than the critical micelle concentration (CMC), which is 1.1 mM [58].

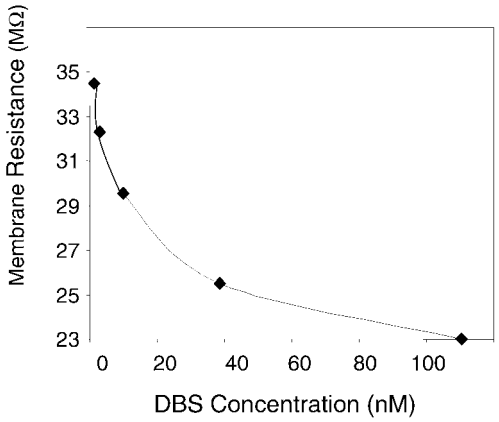

Figure 1.2.13. Plot of membrane resistance versus DBS concentration.

1.2.5.3 Transport Experiments

These were conducted by mounting the membrane between the two halves of a U-tube permeation cell and adding 0.1 M KCl to each half-cell. The feed half-cell was also 50 μM in either $Ru(bpy)_3^{2+}$ or naphthalene disulfonate (NDS^{2-}), the permeate ions. These permeate ions were chosen because transport from the feed solution through the membrane and into the permeate solution can be easily monitored by measuring the UV absorbance of the permeate solution (both permeate ions were detected at 286 nm). Transport occurred by diffusion of the permeate ion down the concentration gradient across the membrane; both the feed and permeate half-cells were vigorously stirred during the permeation experiments.

The experimental protocol used was as follows. An increment of the analyte surfactant (for these experiments DBS) was added to both the feed and permeate half-cells and permeation was allowed to occur for 24 h. After this time, the permeate half-cell was sampled and the UV absorbance was used to determine the moles of the permeate ion transported. The permeate solution was then returned to the permeate half-cell and a second increment of DBS was added. Permeation was again allowed to occur for 24 h and the amount of permeate ion transport was again determined. This process was repeated for various DBS concentrations over the range from 10^{-8} to 10^{-4} M.

The data obtained for $Ru(bpy)_3^{2+}$ transport are shown in Figure 1.2.12. At DBS concentrations below 10^{-6} M there is no detectable $Ru(bpy)_3^{2+}$ in the permeate solution. It is important to emphasize that each permeation data point in Figure 1.2.12 corresponds to an additional 24 h of permeation time. Hence, by the time the DBS concentration was increased to 9×10^{-7} M, the total permeation time was 5 days. The inability to detect $Ru(bpy)_3^{2+}$ in the permeate solution after 5 days of permeation, shows that over the DBS concentration range 0 to $\sim 10^{-6}$ M, the pores in the C_{18} membrane are not wetted by water, making the rate of

$Ru(bpy)_3^{2+}$ transport immeasurable small. These data, again, show that at DBS concentrations below 10^{-6} M, the membrane is in the off state.

At DBS concentrations above 10^{-6} M, $Ru(bpy)_3^{2+}$ transport is switched on, and flux increases with concentration of DBS for concentrations above this value. The impedance and transport data tell a consistent story about the effect of DBS on the C_{18}-derivatized membrane (Figure 1.2.12). At low DBS concentrations ($<10^{-6}$ M) where the membrane resistance is in the $10^7\ \Omega$ range, $Ru(bpy)_3^{2+}$ is not transported. The sudden drop in R_m at DBS concentrations above $\sim 10^{-6}$ M is seen in the transport experiments as an abrupt switching on of $Ru(bpy)_3^{2+}$ transport across the membrane.

In order to understand the nature of this abrupt switch to the 'on' state, we compared $Ru(bpy)_3^{2+}$ and NDS^{2-} fluxes across bare (no C_{18}) alumina membranes with fluxes across C_{18}-modified membranes that had been exposed to 10^{-4} M DBS. The $Ru(bpy)_3^{2+}$ fluxes for the bare alumina membrane and for the C_{18}-modified membrane that had been exposed to 10^{-4} M DBS are the same. In the case of the bare membrane, the pores are flooded with water and transport occurs by diffusion through these water-filled pores. The equivalence of the flux for the C_{18}-modified membrane that had been exposed to 10^{-4} M DBS clearly shows that the pores in this membrane are also flooded with water. The same results were obtained for the flux of the anionic permeate ion NDS^{2-}. An anion was studied to insure that transport of the cationic $Ru(bpy)_3^{2+}$ was not being facilitated in some way by the anionic surfactant incorporated within the pores. Again, these data show that the transition from the off state to the on state occurs because at DBS concentrations above 10^{-6} M, sufficient DBS has partitioned into the membrane that the pores spontaneously flood with water and electrolyte.

1.2.5.4 X-ray Photoelectron Spectroscopy (XPS)

XPS was used to show that the prototypical analyte dodecylbenzene sulfonate (DBS) is present on the C_{18}-modified alumina surface after exposure of the membrane to DBS solution. However, the XPS cross-section for S from the DBS proved too weak to obtain unambiguous evidence; furthermore, O, C, and Na^+ (the counterion for the DBS) are ubiquitous, and therefore not useful as probes to prove that DBS is present on the surface. For this reason, we used a surface ion-exchange reaction to replace Na^+ with Cs^+ as the counterion for the surface-bound DBS. We then used XPS to look for the presence of Cs^+ on the C_{18}-modified surface that had been treated with DBS, using an identical surface that was exposed to the Cs^+ solution but not to DBS as the control.

Figure 1.2.14 shows XPS data for a C_{18}-modified membrane that had been exposed to an aqueous 2.0 mM solution of Na^+-DBS, rinsed, exposed to a 100 mM aqueous solution of $CsNO_3$, and then rinsed extensively again. The Cs 3d peaks at 724 and 738 eV are clearly evident [59]. This may be contrasted with the control surface, a C_{18}-modified alumina membrane that was exposed to the Cs^+ solution but not to DBS, where no Cs signal is seen (Figure 1.2.14). These data

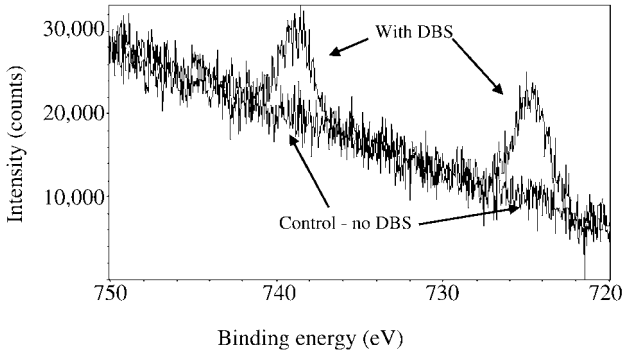

Figure 1.2.14. XPS data for a C_{18}-modified alumina membrane surface that was exposed to a DBS solution and then to a Cs^+ solution and for an identical surface that was exposed to Cs^+ but not to DBS.

show that exposure of the membrane to DBS results in partitioning of this analyte species on to the C_{18}-modified surface.

1.2.5.5 Measurements of Ion Current

While the transport experiments show that the analyte DBS can switch on ion (eg, $Ru(bpy)_3^{2+}$ and NDS^{2-}) transport across the membrane, we also wanted to obtain a direct measure of the ion current. To do this, a constant transmembrane potential of 1.5 V was applied and the resulting transmembrane ion current was measured. The current was monitored for 30 min and then the half-cell solutions were spiked with DBS to a total concentration of 10^{-9} M. The current was again measured for 30 min and the half-cells were spiked again with DBS. This process was repeated for various DBS concentrations over the range from 10^{-9} to $10^{-3.5}$ M.

Figure 1.2.15 shows the measured ion current versus time data; at the indicated times the electrolyte solutions were spiked to the indicated concentrations with DBS. The ion current data show the same general trend as both the impedance and transport data: at concentrations below $\sim 10^{-6}$ M the ion current is at a very low baseline value and at concentrations above $\sim 10^{-6}$ M the ion current abruptly switches on. In addition, the $10^{-5.5}$ M datum shows that the transition from the low-current to the high-current state occurs very abruptly.

Both the impedance and ion current data show that when the membrane is in the off state, some small baseline current does flow across the membrane. It is important to note that the resistance value for the off state obtained by the impedance and ion current measurements are essentially identical. As shown in Figure 1.2.12, the impedance measurement yields a value of $\sim 10^7\ \Omega$. The ion current in the off state is $\sim 1.5\times10^{-7}$ A, which for a 1.5 V transmembrane potential yields a membrane resistance of $\sim 10^7\ \Omega$. The issue left to resolve, however, is

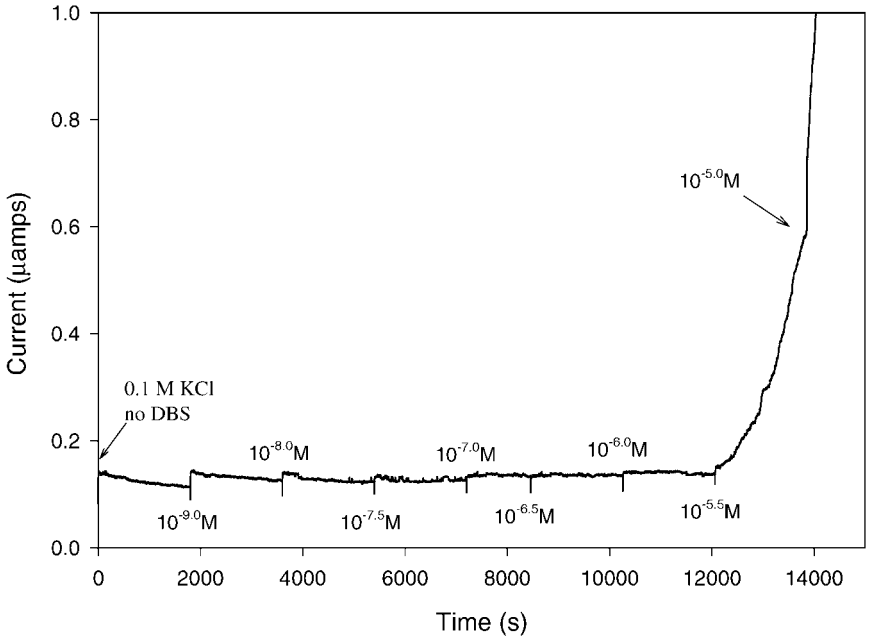

Figure 1.2.15. Ion current through a C_{18}-modified alumina membrane versus time. The contacting solution phases were spiked with the indicated concentrations of DBS at the indicated times. The electrolyte was 0.1 M KCl. A constant transmembrane potential of 1.5 V was applied.

what is supporting this baseline ion current when the membrane is in the off state? At this point we cannot say other than to suggest that this current results from some surface conduction process that occurs along the pore walls when the pores are devoid of water. In the absence of DBS, this surface conduction process may involve residual surface hydroxyl sites. The impedance data (Figure 1.2.12) indicate that in the presence of DBS, the surfactant itself is involved in the conduction process.

1.2.5.6 Effect of Alkyl Chain Length and Nature of the Surfactant Head Group

The above data show that partitioning of the analyte DBS into the membrane is responsible for the transition to the on state. It seems likely that this partitioning process is driven by the hydrophobic effect. To prove this point, C_{18}-modified alumina membranes were exposed to 0.1 wt% solutions of various alkyl sulfonate, alkyl benzene sulfonate, and trimethyl alkyl ammonium surfactants. This 0.1 wt% corresponds to a change in concentration from 8.1 mM for the smallest surfactant to 2.8 mM for the largest. The membranes were then rinsed with water

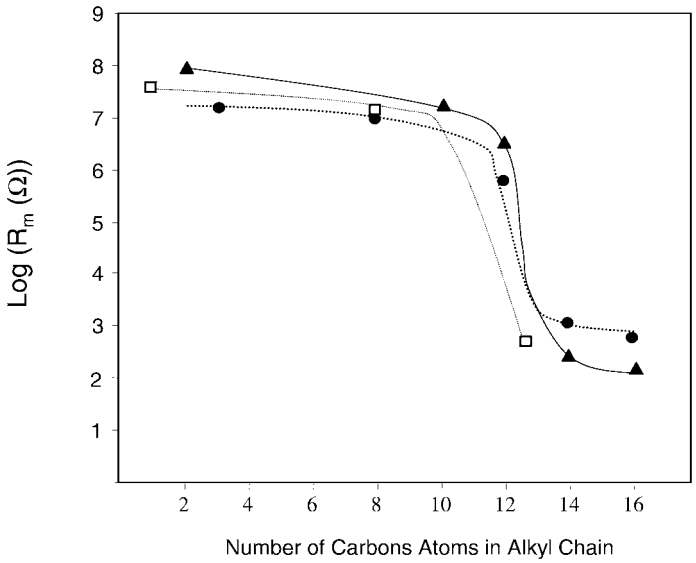

Figure 1.2.16. Plots of log(membrane resistance) for C_{18}-modified alumina membranes as a function of the carbon chain length of the surfactant exposed to the membrane. Prior to measurement, the membranes were soaked in 0.1 wt% surfactant solutions. □, Benzenesulfonate; ●, sulfonate; ▲, trimethylammonium surfactant families.

and the impedances determined in 0.1 M KCl that was devoid of surfactant. Figure 1.2.16 shows plots of log (membrane resistance) versus number of carbon atoms in the alkyl side chain for all of the surfactants investigated. These data show that in order for a surfactant to switch the membrane to the on state, the alkyl chain must be above some minimum length. For the alkyl benzenesulfonates, a 12-carbon chain is required. For the alkyl sulfonates and alkylammoniums, the alkyl group must be at least 14 carbons long (Figure 1.2.16).

These data clearly show that the hydrophobic effect is responsible for driving the surfactant into the C_{18}-modified membrane. The difference between the alkyl benzenesulfonates and the other two classes of surfactants reflects the added contribution of the benzene group to the hydrophobicity. With the added benzene group, a 12-carbon alkyl chain can switch the membrane to the on state; without the benzene group a 14-carbon chain is needed (Figure 1.2.16). The data in Figure 1.2.16 also show that for the long-chain surfactants the adsorption of the surfactant to the membrane is essentially irreversible if the membrane is exposed to aqueous solution. However, we have found that the surfactant can be removed from the membrane by rinsing with ethanol. After the ethanol rinse the membrane resistance returns to values equivalent to the off state obtained prior to exposure to surfactant.

1.2.5.7 Detection of Drug Molecules

To explore further the role of the hydrophobic effect in driving the analyte species into the C_{18}-derivatized alumina membrane, we investigated the effect of hydrophobic cationic drug molecules on the membrane resistance. The molecules and their molecular weights are amiodarone (645 g mol^{-1}), amitriptyline (278 g mol^{-1}), and bupivacaine (288 g mol^{-1}) (Figure 1.2.17). Because its molecular weight is more than double those of the other drugs and because it contains very hydrophobic iodo substituents, amiodarone is by far the most hydrophobic of these molecules. If the hydrophobic effect is responsible for driving molecules into the C_{18}-derivatized membrane, then the transition from the off to the on state would occur at lowest concentrations for amiodarone, and this is what is observed experimentally (Figure 1.2.17). There is only a 3% difference in the molecular weights of amitriptyline and bupivacaine; however, bupivacaine presents two additional opportunities for hydrogen bonding with water: the lone pairs on the carbonyl group and the lone pair of the nonprotonated nitrogen. For this reason, bupivacaine is much more hydrophilic, and it would be expected to be the mostly poorly detected of the three drugs; Figure 1.2.17 shows that this is also observed experimentally.

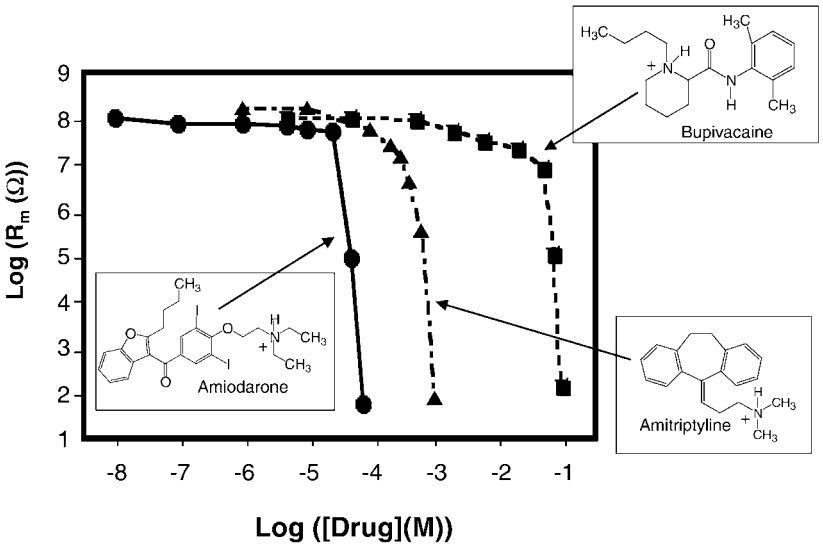

Figure 1.2.17. Plots of log(membrane resistance) versus log[drug] for the indicated drugs and a C_{18}-modified alumina membrane.

1.2.5.8 Switching the Membrane in Response to Solution pH

We have also investigated the effect of solution pH on the resistance of a membrane that was derivatized with the hydrophobic carboxylated silane –Si–$(CH_2)_3$NHCO–$(CH_2)_{20}$–COOH. At low pH values, the membrane resistance is high ($>10^5\ \Omega$), signifying the off state (Figure 1.2.18). That the resistance of the off state for this membrane is lower than that for the C_{18}-derivatized membrane is not surprising because the 18-carbon alkyl chain is certainly more hydrophobic than the –$(CH_2)_3$NHCO–$(CH_2)_{20}$–COOH chain. A small but measurable decrease in membrane resistance with increasing pH is observed over the pH range 5.5–8.0. Above pH 8 there is a large (more than four orders of magnitude) drop in membrane resistance, signifying the transition to the on state. The membrane resistance after this pH is, in fact, indistinguishable from that of the bare alumina membrane, of the order of 5 Ω.

The transition to the on state is associated with the deprotonation of the carboxylic acid group. This is a reversible effect; the fully deprotonated membrane obtained after exposure to pH 10 buffer can be rinsed and dried and then re-exposed to pH 5.5 buffer to regenerate the off state of the membrane. Finally, if it is assumed that the surface-bound long chain carboxylic acid has a typical aqueous solution phase K_a ($\sim 10^{-5}$), then the transition to the on state occurs when 99.9% of the –COOH groups have been deprotonated. This is, however, only an approximation because the very hydrophobic environment within the silane-modified pores may substantially change the K_a relative to the solution value. In fact, when Kane and Mulvaney [60] and Hu and Bard [61] examined the pK_as of aliphatic carboxylic acids in well-formed monolayers, they found an increase of 2–3 units in the pK_a values. This may account for the on state of our membrane occurring at pH 8.

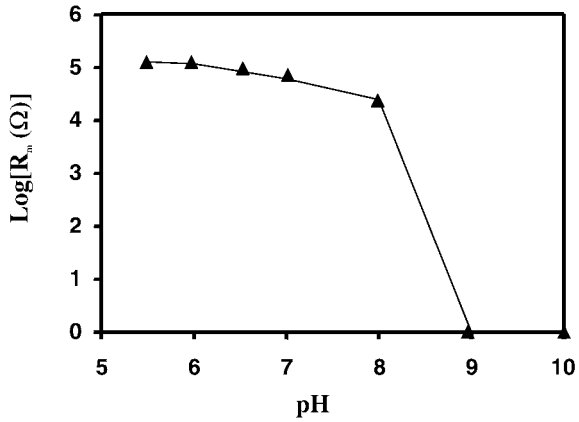

Figure 1.2.18. Plots of log(membrane resistance) versus pH for a –$(CH_2)_3$NHCO–$(CH_2)_{20}$–COOH-modified alumina membrane.

1.2.5.9 Effect of Pore Density and Pore Diameter on Analyte Detection

Au nanotube membranes that were rendered hydrophobic by chemisorbing octadecanethiol [11] were used to explore these issues. These membranes contained ~ 2 nm id Au nanotubes and had a total porosity of only 2×10^{-3}%. This may be contrasted with the alumina membranes which contain pores that are two orders of magnitude larger in diameter and are ~ 30% porous. In a study analogous to Figure 1.2.12, we examined the resistance of these membranes with increasing concentration of DBS. An abrupt transition from a very high-resistance off state to a four orders of magnitude lower resistance on state is observed over essentially the same concentration range as is observed for the C_{18}-derivatized alumina membranes (Figure 1.2.19).

These results show that for membranes containing either C_{18}-modified alumina micropores or C_{18}-modified Au nanotubes, the concentration of DBS that induces the transition from the off to the on state does not depend on porosity or pore/tube diameter. Although at first glance this may seem surprising, it is important to point out that changing the porosity or pore/nanotube diameter in reality changes only the surface area of C_{18} groups available for the adsorption of analyte, ie, the low-porosity Au nanotube membranes have a lower surface area available for analyte adsorption than the alumina membranes. This situation can be modeled by assuming that the analyte is adsorbed on the C_{18}-modified surfaces via a Langmuir isotherm and that a certain critical fraction (Θ_c) of the surface must be covered with analyte in order to flood the pores with electrolyte. Θ_c is related to the equilibrium constant for the adsorption reaction (β) and the activity of DBS in the solution phase (a_{DBS}) via [62]

$$\Theta_c = (\beta a_{DBS})/(1 + \beta a_{DBS}) \tag{1.2.7}$$

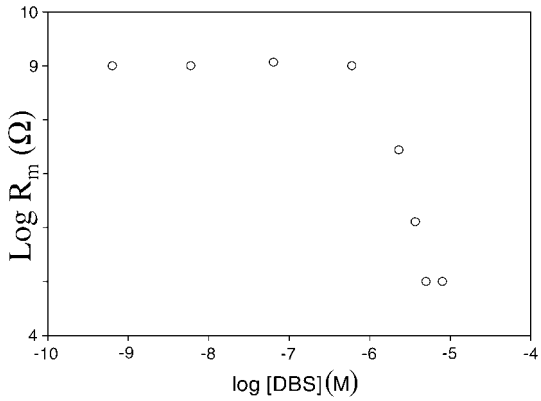

Figure 1.2.19. Plots of log(membrane resistance) versus log[DBS] for a C_{18}-modified Au nanotube membrane.

Equation (1.2.7) shows that Θ_c depends only on the value of the equilibrium constant (the same for both membranes, since both contain C_{18} alkyl groups) and the activity of surfactant in solution. Because surface area does not enter into the equation, the concentration of DBS required to switch the membrane to the on state should be independent of membrane porosity and pore diameter, and this is what is observed experimentally.

1.2.6 Conclusion

In this review, we have discussed the use of Au nanotube membranes to separate molecules on the basis of size. Furthermore, we have described a highly sensitive method of electroanalysis based on these membranes. Besides showing size-based selectivity, previous studies have demonstrated that these Au nanotube membranes can show ionic charge-based transport selectivity and that the membranes can be electrochemically switched between anion-transporting and cation-transporting states [45]. Hence these membranes can be viewed as universal ion exchangers. Furthermore, chemical transport selectivity can be introduced into these membranes by chemisorbing thiols to the inside tube walls [10, 11]. In this case, the chemisorbed thiol changes the chemical environment within the nanotubes and this, in turn, changes the transport properties of the membrane. For example, membranes modified with hydrophobic thiols selectively transport hydrophobic molecules [11]. Hence these nanotube membranes can utilize all of the selectivity paradigms (sterics, electrostatics, and chemical interactions) that Nature uses in the design of exquisitely selective molecular recognition schemes (eg, protein [63] and ion channels [42]). Nanotube membranes can be viewed as model systems for these naturally-occurring nanotubes. Indeed, we have shown that synthetic micropore and nanotube membranes can mimic the function of ligand-gated ion channels, ie, they can be switched from an off state to an on state in response to the presence of a chemical stimulus. This concept of ion channel mimetic sensing, as originally proposed by Umezawa's group [64], has been of considerable interest in analytical chemistry [65–67]. There is also considerable appeal in using naturally occurring and genetically engineered protein channels as sensors (see [45] and references therein). Such research at the bio/nano interface is of great current interest in our group.

1.2.7 Acknowledgement

Aspects of this work were supported by the Office of Naval Research and the National Science Foundation.

1.2.8 References

[1] Martin, C.R., *Science* **266** (1994) 1961–1966.
[2] Hulteen, J.C., Martin, C.R., *J. Mater. Chem.*, **7** (1997) 1075–1087.
[3] Martin, C.R., Mitchell, D.T., *Anal. Chem.*, **70** (1998) 322A–327A.
[4] Fleischer, R.L., Price, P.B., Walker, R.M., *Nuclear Tracks in Solids*; Berkeley, CA: University of California Press, 1975.
[5] Hornyak, G.L., Patrissi, C.J., Martin, C.R., *J. Phys. Chem. B.*, **101** (1997) 1548–1555.
[6] Possin, G.E., *Rev. Sci. Instrum.*, **41** (1970) 772.
[7] Williams, W.D., Giordano, N., *Rev. Sci. Instrum.*, **55** (1984) 410.
[8] Nishizawa, M., Menon, V.P., Martin, C.R., *Science*, **268** (1995) 700–702.
[9] Jirage, K.B., Hulteen, J.C., Martin, C.R., *Science,* **278** (1997) 655–658.
[10] Hulteen, J.C., Jirage, K.B., Martin, C.R., *J. Am. Chem. Soc.,* **120** (1998) 6603–6604.
[11] Jirage, K.B., Hulteen, J.C., Martin, C.R., *Anal. Chem.,* **71** (1999) 4913–4918.
[12] Hou, Z., Abbott, N.L., Stroeve, P., *Langmuir,* **16** (2000) 2401–2404.
[13] Tourillon, G., Pontinnier, L., Levy, J.P., Langlais, V., *Electrochem. Solid-State Lett.,* **3** (2000) 20–23.
[14] Schonenberger, C., van der Zande, B.M.I., Fokkink, L.G.J., Henry, M., Schmid, C., Kruger, M., Bachtold, A., Huber, R., Birk, H., Staufer, U., *J. Phys. Chem. B,* **101** (1997) 5497–5505.
[15] Preston, C.K., Moskovits, M.J. *J. Phys. Chem.,* **97** (1993) 8405.
[16] Martin, C.R., in: *Handbook of Conducting Polymers*, 2nd edn., Reynolds, J.R., Skotheim, T., Elsebaumer, R. (eds.); New York: Marcel Dekker, 1997, Chap. 16, pp. 409–421.
[17] Duchet, J., Legras, R., Demoustier-Champagne, S., *Synth. Met.,* **98** (1998) 113–122.
[18] Demoustier-Champagne, S., Stavaux, P.-Y., *Chem. Mater.,* **11** (1999) 829–834.
[19] Sukeerthi, S., Contractor, Q., *Anal. Chem.,* **71** (1999) 2231–2236.
[20] Lakshmi, B.B., Patrissi, C.J., Martin, C.R., *Chem. Mater.*, **9** (1997) 2544–2550.
[21] Lakshmi, B.B., Dorhout, P.K., Martin, C.R., *Chem. Mater.,* **9** (1997) 857–862.
[22] Che, G., Lakshmi, B.B., Martin, C.R., Fisher, E.R., *Langmuir,* **15** (1999) 750–758.
[23] Che, G., Fisher, E.R., Martin, C.R., *Nature*, **393** (1998) 346–349.
[24] Kyotani, T., Tsai, L.F., Tomita, A., *Chem. Commun.* (1997) 701.
[25] Patrissi, C.J., Martin, C.R., *J. Electrochem. Soc.*, **146** (1999) 3176–3180.
[26] Li, N., Patrissi, C.J., Martin, C.R., *J. Electrochem. Soc.,* **147** (2000) 2044–2049.
[27] Che, G., Jirage, K.B., Fisher, E.R., Martin, C.R., Yoneyama, H., *J. Electrochem. Soc.,* **144** (1997) 4296–4302.
[28] Cepak, V.M., Hulteen, J.C., Che, G., Jirage, K.B., Lakshmi, B.B., Fisher, E.R., Martin, C.R., *J. Mater. Res.*, **13** (1998) 3070–3080.
[29] Cepak, V.M., Hulteen, J.C., Che, G., Jirage, K.B., Lakshmi, B.B., Fisher, E.R., Martin, C.R., *Chem. Mater.,* **9** (1997) 1065–1067.
[30] Martin, B.R., Dermody, D.J., Reiss, B.D., Fang, M., Lyon, L.A., Natan, M.J., Mallouk, T.E., *Adv. Mater.,* **11** (1999) 1021–1025.
[31] Penner, R.M., Martin, C.R., *Anal. Chem.,* **59** (1987) 2625–2630.
[32] Cheng, I.F., Martin, C.R., *Anal. Chem.*, **60** (1988) 2163–2165.
[33] Menon, V.P., Martin, C.R., *Anal. Chem.,* **67** (1995) 1920–1928.

[34] Hulteen, J.C., Menon, V.P., Martin, C.R., *J. Chem. Soc., Faraday Trans. 1,* **92** (1996) 4029–4032.
[35] Kang, M.S., Martin, C.R., *Langmuir.* **17** (2001) 2753–2759.
[36] Lee, S.B., Martin, C.R., *Anal. Chem.*, **73** (2001) 768–775.
[37] Parthasarathy, R.V., Menon, V.P., Martin, C.R., *Chem. Mater.*, **9** (1997) 560–566.
[38] Chen, W.-J., Martin, C.R., *J. Membr. Sci.,* **104** (1995) 101–108.
[39] Liu, C., Martin, C.R., *Nature,* **352** (1991) 50–52.
[40] Kobayashi, Y., Martin, C.R., *Anal. Chem.*, **71** (1999) 3665–3672.
[41] Kobayashi, Y., Martin, C.R., *J. Electroanal. Chem.*, **431** (1997) 29–33.
[42] Voet, D., Voet, J.G., *Biochemistry*, 2nd edn.; New York: Wiley, 1995, pp. 1297–1298.
[43] Steinle, E.D., Mitchell, D.T., Wirtz, M., Lee, S.B., Young, V.Y., Martin, C.R., *Anal. Chem.*, in press.
[44] Kathawalla, I.A., Anderson, J.L., Lindsey, J.S., *Macromolecules,* **22** (1989) 1215–1219.
[45] Martin, C.R., Nishizawa, M., Jirage, K.B., Kang, M.S., *J. Phys. Chem. B,* **105** (2001) 1925–1934.
[46] Bayley, H., Martin, C.R., *Chem. Rev.,* **100** (2000) 2575–2594.
[47] Deen, V.M., *AICHE J.,* **33** (1987) 1409–1425.
[48] Nitsche, J.M., Balgi, G., *Ind. Eng. Chem. Res.,* **33** (1994) 2242–2247.
[49] Archibald, D.D., Qadri, S.B., Gaber, B.P., *Langmuir,* **12** (1996) 538–546.
[50] Cohen, Y., Levi, S., Rubin, S., Willner, I., *J. Electroanal. Chem.,* **417** (1996) 65–75.
[51] Armstrong, R.D., Covington, A.K., Evans, G.P., *J. Electroanal. Chem.,* **159** (1983) 33–40.
[52] Xie, S.-L., Cammann, K., *J. Electroanal. Chem.,* **229** (1987) 249–263.
[53] Zhang, W., Spichiger, U.E., *Electrochim. Acta,* **45** (2000) 2259–2266.
[54] Ding, L., Li, J., Dong, S., Wang, E., *J. Electroanal. Chem.,* **416** (1996) 105, **112.**
[55] Ikematsu, M., Iseki, M., Sugiyama, S., Mizukami, A., *Biosystems,* **35** (1995) 123–128.
[56] Calistri-Yeh, M., Kramer, E.J., Sharma, R., Zhao, W., Rafailovich, M.H., Sokolov, J., Brock, J.D., *Langmuir,* **12** (1996) 2747–2755.
[57] Pursch, M., Vanderhart, D.L., Sander, L.C., Gu, X., Nguyen, T., Wise, S.A., Gajewski, D. A., *J. Am. Chem. Soc.,* **122** (2000) 6997–7011.
[58] Ohki, K., Tokiwa, F., *J. Chem. Soc. Jpn. Chem. Ind. Chem.,* **91** (1970) 534–539.
[59] Muilenberg, G.E. (ed.), *Handbook of X-Ray Photoelectron Spectroscopy*; Eden Prairie: Perkin-Elmer, 1978.
[60] Kane, V., Mulvaney, P., *Langmuir,* **14** (1998) 3303–3311.
[61] Hu, K., Bard, A.J., *Langmuir,* **13** (1997) 5114–5119.
[62] Bard, A.J., Faulkner, L.R., *Electrochemical Methods*; New York: Wiley, 1980.
[63] Bayley, H., *Sci. Am.*, September (1997) 62.
[64] Sugawara, M., Kojima, K., Sazawa, H., Umezawa, Y., *Anal. Chem.,* **59** (1987) 2842–2846.
[65] Xiao, K.P., Bühlmann, P., Umezawa, Y., *Anal. Chem.,* **71** (1999) 1183–1187.
[66] Wu, Z., Tang, J., Cheng, Z., Yang, X., Wang, E,. *Anal. Chem.,* **72** (2000) 6030–6033.
[67] Katayama, Y., Ohuchi, Y., Yang, X., Wang, E., *Anal. Chem.*, **72** (2000) 4671–4674.

List of Symbols and Abbreviations

Symbol	Designation
a_{DBS}	activity of DBS in solution phase
C	membrane capacitance
D	diffusion coefficient
i	transmembrane current
I	membrane thickness
k	Boltzmann constant
M	molecular weight
n	number of nanotubes in membrane
P	pressure
Q	gas flux
r	radius of nanotubes
r_m	molecular radius
r_{tube}	radius of nanotube
R	resistance
T	absolute temperature
α	selectivity coefficient
β	equilibrium constant for adsorption reaction
η	viscosity
λ	ratio of radius of diffusing molecule to radius of nanotube
Θc	critical fraction of surface

Abbreviation	Explanation
CMC	critical micelle concentration
DBS	1-dodecanesulfonic acid
XPS	x-ray photoelectron spectroscopy